Characteristics of Coastal-Trapped Waves Induced by Typhoon along the Southeast Coast of Honshu, Japan

Yosuke Igeta*, Yujiro Kitade and Masaji Matsuyama

Department of Ocean Sciences, Faculty of Marine Science, Tokyo University of Marine Science and Technology, Konan, Minato-ku, Tokyo 108-8477, Japan

Mooring observations using ADCP, electromagnetic current meters and thermometers were performed to clarify the vertical and horizontal structure of coastal-trapped waves (CTWs) on continental shelf and slope on the eastern side of Sagami Bay, Japan, in August and September 2003. A strong inflow associated with CTW caused by Typhoon 0315 (CTW15) was observed with remarkable downwelling. The maximum current due to CTW15 was over 100 cm s^{-1}, confined to the upper layer shallower than 90 m. The CTW (CTW10) induced by Typhoon 0310, was associated with the coastal upwelling and maximum outflow was 33 cm s^{-1}; the currents were extended near the bottom at 230 m depth. Remarkable discrepancies were found between the current structures of CTWs. CTW15 was explained by superposing the second CTW mode on the first CTW mode, whereas CTW10 was explained by the first CTW mode. The generation and propagation processes of both CTWs were reproduced by numerical experiments using a three-dimensional level model. The model results indicated that the difference of modal characteristics between CTW15 and CTW10 already exists in the CTW generation region and are due to difference of the wind direction, i.e., the typhoon's path.

1. Introduction

Coastal-trapped waves (CTWs) have been observed on continental shelf and slope regions in a stratified ocean (e.g. Gill, 1982). Properties of the CTW are roughly classified by the stratification parameter, $\varepsilon = \lambda/L$, where λ is an internal radius of deformation and L is shelf width. The CTW has characteristics of an internal Kelvin wave for $\varepsilon > 1$, while it has characteristics of a continental shelf wave for $\varepsilon \ll 1$ (Kajiura, 1974; Wang and Mooers, 1976). Both types of CTW have been observed along the southeast coast of Honshu, Japan. Kubota *et al.* (1981) found current and sea-level fluctuations with a 100-hour period off the Fukushima coast (Fig. 1(a)) where the continental shelf is wide. From a numerical experiment, Kubota (1985) indicated that the fluctuations were due to the continental shelf waves induced by wind. In Sagami Bay, where the continental shelf is very narrow (Fig. 1), Kitade

et al. (1998) found CTW with characteristics of the internal Kelvin wave from mooring observations at six stations. Kitade and Matsuyama (2000) performed numerical experiments using a two-layer model, which indicated that the CTW changes its wave properties from the continental shelf wave to the internal Kelvin wave off the southeast coast of the Boso Peninsula (Fig. 1), where the shelf width rapidly narrows.

Abnormal stormy currents in Sagami Bay (Fig. 1), "*Kyucho*", are known to occur after a typhoon's passage and occasionally break fishing set-nets along the coast (e.g. Ishidoya, 2001). Matsuyama *et al.* (1997) observed the stormy current by mooring observation at one current measurement station and three temperature measurement stations after passage of Typhoon 8818. They showed that the stormy current was accompanied by a steep temperature rise, and moved cyclonically around Sagami Bay with a propagation speed of 0.6 m s^{-1}. Igeta *et al.* (2003) performed a numerical experiment using a three-dimensional level model and showed that the stormy current due to CTW was caused along the east coast of the Boso Peninsula by the strong southward wind of the typhoon. However, the detailed vertical current structures of CTWs and its time variations have not been observed along the south-

---

* Corresponding author. E-mail: igeta@affrc.go.jp

Present address: Japan Sea National Fisheries Research Institute, Fisheries Research Agency, Suido-cho, Chuo-ku, Niigata-shi, Niigata 951-8121, Japan.
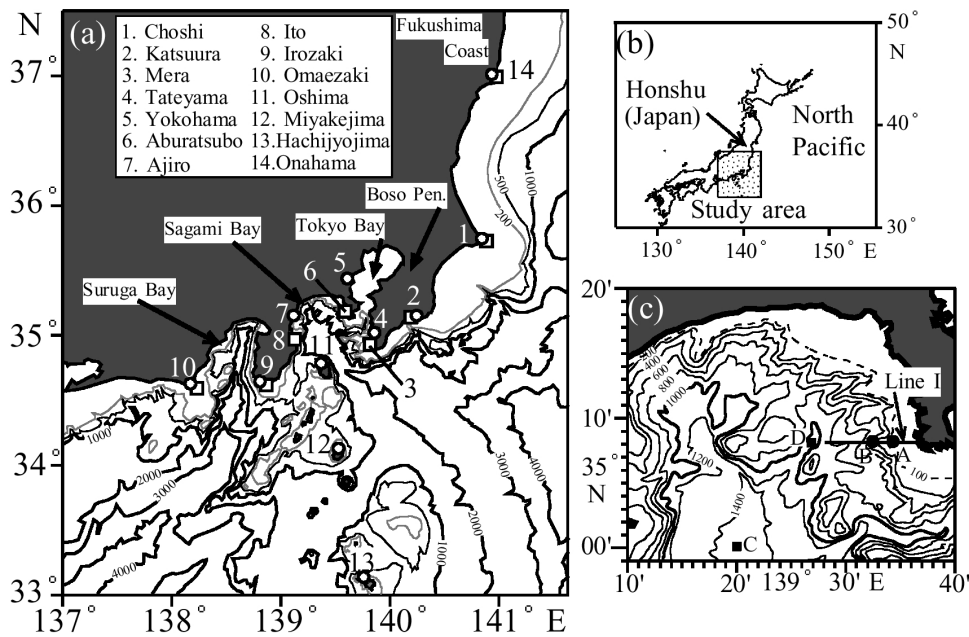
Fig. 1. (a) Bathymetry chart of the southeast of Japan. (b) Location of the study area. (c) Bottom topography in Sagami Bay. Locations of meteorological and tidal stations are indicated by open circles and open squares, respectively. Closed circles and closed squares indicate mooring observation sites and the CTD stations, respectively. Mode structure along Line I is investigated.

east coast of Honshu, Japan. In addition, the modal characteristics of CTW generated by strong wind stress have not been clarified by observational results.

We performed ADCP (acoustic Doppler current profiler) current measurements at two mooring stations on the eastern side of Sagami Bay in 2003. During the observation period, two typhoons passed near the mooring stations (Fig. 2). Typhoon 0310 (hereinafter T10) moved over Honshu in August and Typhoon 0315 (hereinafter T15) passed south off Sagami Bay in the middle of September. The detailed vertical structures of two CTWs induced by T10 and T15 were obtained by the measurements. In addition, remarkable differences of current structures were found between both CTWs.

In this study, we investigated the current structures of the CTWs by modal decompositions and tried to clarify the formation processes of the different modal characteristics of the CTWs by numerical experiments. Section 2 outlines the observations and the data, and Section 3 describes details of the two remarkable CTWs induced by typhoons, and the modal characteristics of the CTWs are investigated based on the free baroclinic CTW theory. Section 4 describes the numerical experiments performed using a three-dimensional level model to investigate the differences of modal characteristics of the CTWs. Section 5 compares the model results with the observational ones, and the formation processes of the different current
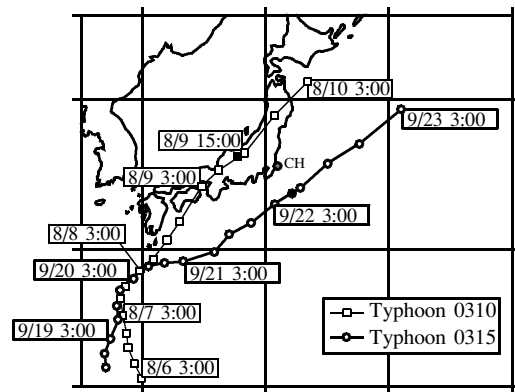

Fig. 2. Tracks of Typhoon 0310 (thin line with open squares) and Typhoon 0315 (thick line with open circles). Closed square and closed circle indicate the locations of the center of the typhoons when the wind speed was maximum at Choshi (CH).

structures of the two CTWs are discussed. Section 6 is a summary.

2. Observation and Data

Current and temperature observations were conducted at Sta. A (35°08′ N, 139°34′ E, water depth of 93

m), located at the shelf edge, and Sta. B (35°08′ N, 139°32′ E, water depth of 250 m), located at the continental slope, in Sagami Bay (Fig. 1) from 28 July to 6 October 2003. Workhorse ADCP (300 kHz; RD Instruments) and temperature-depth sensors were mounted on the sea bottom at Sta. A, while a mooring system with a workhorse ADCP (300 kHz; at 148 m depth), electromagnetic current meters (ACM, at 165, 190 and 236 m depths), memory thermometers (at 111, 121 and 131 m depths), and temperature-depth meter (at 103 m depth) were deployed at Sta. B. Both ADCPs were set up with 4-m bin resolution in the vertical. The sampling interval was 3 minutes for the ADCP and the thermometer, and 10 minutes for the ACM and temperature-depth meter. All the current and temperature data were subsampled every 30 minutes for use in the present study. Subtidal fluctuations of current and temperature were obtained by applying a low-pass filter with a half-power point of 30 hours (Walters and Heston, 1982).

The depth sensor deployed at the top of the mooring system at Sta. B usually indicated about 103 m, whereas the maximum value was 107 m in the period of a strong current. Depth variation of each sensor on the mooring system at Sta. B was estimated to be about 4 m at most. Therefore, we judged that the depth variations of the current meters can be neglected for the analysis in the present study.

Hourly sea-level data at Onahama, Choshi, Katsuura, Mera, Aburatsubo, Ito, Irozaki, and Omaezaki (Fig. 1), offered by Geographical Survey Institute and Japan Oceanographic Data Center, were used for the CTW analysis. The atmospheric pressure and wind data obtained at one hour intervals at Choshi, Kastuura, Tateyama, Yokohama, Ajiro, Oshima, Irozaki, Omaezaki, Miyakejima and Hachijyojima (Fig. 1), offered by Japan Meteorological Agency, were also used. The subtidal sea-level fluctuations were obtained by removing the diurnal and semi-diurnal tidal components with a tide-killer filter (Hanawa and Mitsudera, 1985), after removing the effects of atmospheric pressure.

The vertical profiles of temperature and salinity were obtained by CTD (Falmouth Scientific, Inc.) measurements at Sta. C on 7 August, and at Sta. D on 13 September 2003 by the TR/V *Seiyo-Maru*, belonging to Tokyo University of Fisheries (the current Tokyo University of Marine Science and Technology).

3. Observational Results

3.1 Current and temperature fluctuations

Figure 3 shows the time variations of the current and temperature at Stas. A and B during the entire observation period. The time variations of atmospheric pressure and wind vectors at Choshi are also indicated at the top
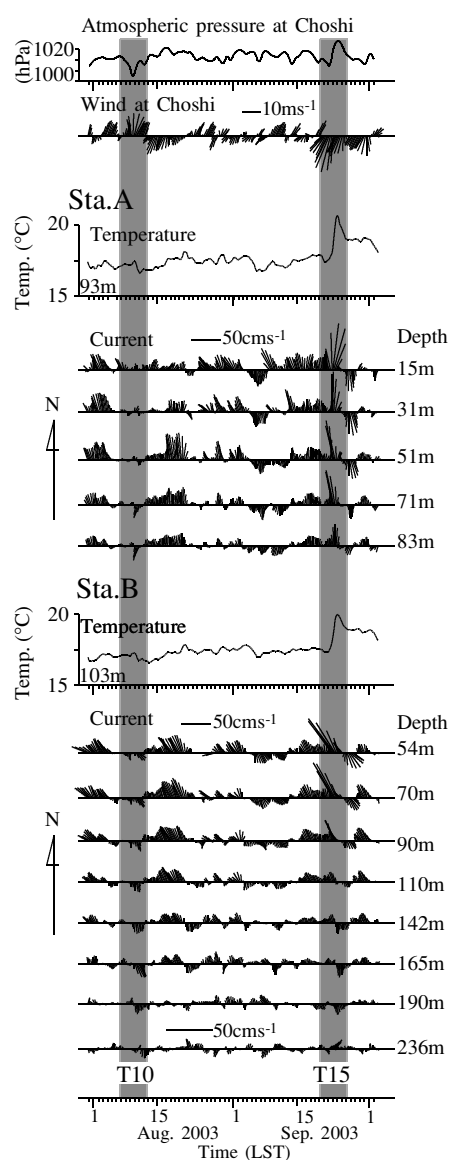

Fig. 3. Time variations of low-pass filtered atmospheric pressure and wind vector at Choshi, temperature and current vector at representative depths at Stas. A and B. Shaded areas indicate the period when Typhoon 0310 (T10) and Typhoon 0315 (T15) had passed, respectively. LST indicate local sidereal time.

of this figure. The northward currents were dominant and intensified at times. The current fluctuations with several-day period were predominant at both stations and similar to each other above 90 m depth. The current and temperature fluctuations were seen to be related with the wind at Choshi. The current and temperature fluctuations with several-day period were most likely caused by CTW induced by the northward wind, as mentioned by Kitade *et al*. (1998) and Kitade and Matsuyama (2000).

In this study we focus on the current variations related to T10 and T15, i.e., the phenomena expected to be induced by strong winds. The southward currents are found at 71 and 83 m depths at Sta. A and throughout the observational depths at Sta. B on 10 and 11 August, during the period of T10's passage. A sudden temperature drop was found at both stations when the southward current appeared. On the other hand, a strong northward current was found above 90 m depth, reaching 100 cm s^{-1} at 15 m depth at Sta. A on 22 September, during the period of T15's passage. A significant temperature rise also appeared together with the northward current, and a high temperature lasted about four days after the significant temperature rise. Details of the current and temperature structures related to T10 and T15 are described with sea level fluctuations in the following subsection.

3.2 Current and temperature structures related to the typhoon's passage

Fluctuations related to T15's passage

The structures of alongshore current and temperature at Stas. A and B during the period of T15 passage are shown in Fig. 4 together with the sea level fluctuations at eight tidal stations along the southeast coast of Honshu. The wind vectors at Choshi are also indicated at the top of this figure. T15 progressed northeastward, to the south of Sagami Bay. The southward wind associated with T15 blew from 20 September to 25 September, and the maximum wind speed was 19 m s^{-1} at 7:00 on 22 September. The alongshore current at 15 m depth at Sta. A shows a strong inflow (northward current) reaching 98 cm s^{-1} at 21:00 on 22 September. The strong inflow was almost uniform above 80 m depth at Sta. A and it rapidly decreasesed with depth near the bottom. A strong inflow was also found above 90 m depth at Sta. B. The current at Sta. B located at the continental slope weakened below 100 m depth and its direction reversed at about 170 m depth when the inflow was at a maximum in the surface layer. The depth of the outflow (southward current) region then shallowed with time. The downward displacement of isotherms indicates downwelling during the period of the strong current in the surface layer, and exceeds 50 m in the observational layer.

The sea level variations show the westward propagation of sea level elevation after T15's passage. The mean propagation speed of the sea level elevation was estimated as about 1.6 m s^{-1} along the coast. At Aburatsubo near the mooring stations, the maximum sea level elevation was observed at 13:00 on 23 September and lagged behind the inflow maximum at 15 m depth by 17 hours, which leading the temperature rise at Sta. A by 5 hours.

The characteristics of current, temperature and sea level fluctuations after T15's passage agree well with these observed by Matsuyama *et al.* (1997) in terms of their
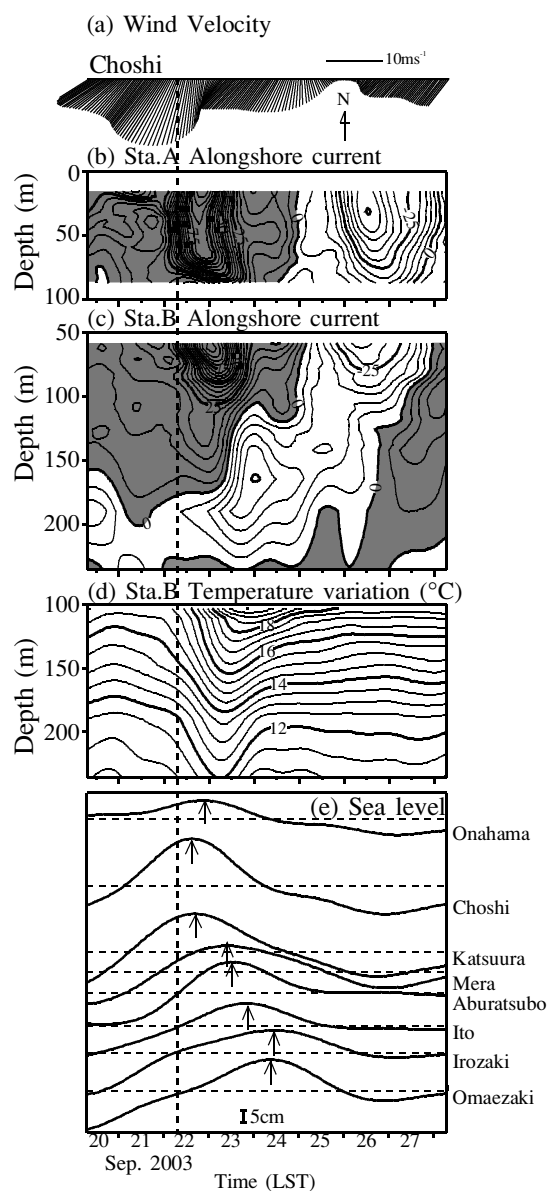

Fig. 4. Time variations of low-pass filtered (a) wind vector at Choshi, (b) alongshore current at Sta. A, (c) alongshore current at Sta. B, (d) temperature at Sta. B, and (e) tidekiller filtered sea level at each tidal station during the period of T15 passage. Shaded areas in (b) and (c) indicate the inflow into Sagami Bay. Vertical dashed line indicates when the maximum wind speed was observed at Choshi.

time variations. Therefore, this phenomenon was considered to be a CTW accompanied by downwelling induced by a southward wind associated with T15, as mentioned by Igeta *et al.* (2003). In this study we call this phenomenon CTW15.

Fluctuations related to T10's passage
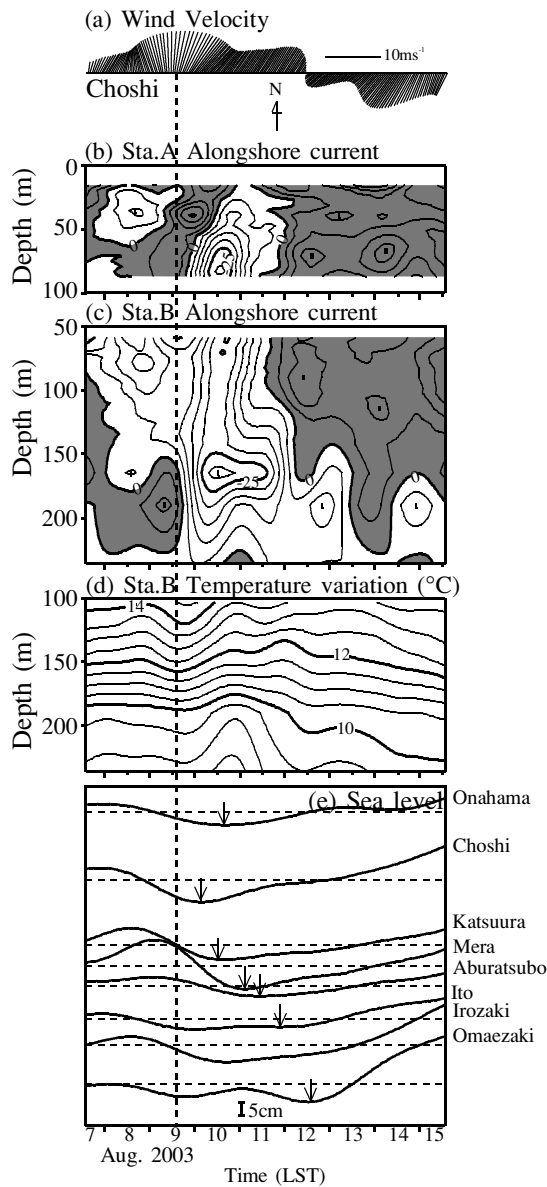
T10 progressed northeastward over Honshu. The

(a) Wind Velocity

Choshi

N

(b) Sta.A Alongshore current

(c) Sta.B Alongshore current

(d) Sta.B Temperature variation (°C)

(e) Sea level

Onahama

Choshi

Katsuura
Mera
Aburatsubo
Ito
Irozaki
Omaezaki

5cm

7 8 9 10 11 12 13 14 15
Aug. 2003
Time (LST)

Fig. 5. As Fig. 4, but for T10 passage.

northward wind associated with T10 blew from 7 August to 12 August and the maximum wind speed was 12.5 m s^{-1} at 14:00 on 9 August at Choshi (Fig. 5). The wind direction was opposite to that of T15. The weak southward currents with a temperature fall were found at both stations. The maximum alongshore current of 28 cm s^{-1} was recorded at 79 m depth at Sta. A at 12:00 on 14 August. The outflow was found throughout the observed layer at Stas. A and B. The maximum outflow appeared above the bottom at Sta. A and at about 160 m depth at Sta. B. The outflow from Sagami Bay was intensified near the bottom at Sta. A, while it was almost uniform from 50 m to 150 m depths and gradually decreased from 150

m depth to the bottom at Sta. B. The outflow was accompanied by slight temperature variations above 170 m depth, and by weak upwelling below 170 m depth. The sea level depression was found together with these current and temperature fluctuations. The sea level depression is seen to propagate westward from Choshi, and its mean propagation speed is estimated as about 1.3 m s^{-1}.

From knowledge gained from previous studies (e.g. Kitade and Matsuyama, 2000), this phenomenon is also considered to be a CTW accompanied by the upwelling induced by the northward wind of T10, and in thus called CTW10 hereinafter.

3.3 Modal characteristics of the coastal-trapped waves

The current measurements on the continental shelf and slope in Sagami Bay indicate detailed current structures associated with CTW15 and CTW10. The current and temperature structures were clearly different between CTW10 and CTW15 as follows: (1) On the continental shelf (Sta. A), the inflow due to CTW15 was very strong and the strong current was concentrated in the surface layer, whereas the outflow due to CTW10 was not so strong and intensified near the bottom; (2) On the continental slope (Sta. B), the current direction of CTW15 was changed vertically, but that of CTW10 was almost uniform throughout the water column; (3) On the continental slope, CTW15 was accompanied by remarkable downwelling throughout the water column, but CTW10 was accompanied by weak upwelling only near the bottom. We focus on the differences in the structures of the CTWs.

To that end, we decomposed the observed current into several CTW modes to characterize the current structure difference between CTW15 and CTW10. A continuously stratified, Bousineseq, f-plane, linearized ocean is assumed. A straight coastline is taken along the y-axis, the x-axis is directed offshore from the coast, while the z-axis is directed upward from the sea surface. The depth profile and stratification are assumed to be independent of the alongshore position (y), the wave frequency is smaller than the inertial frequency, and the alongshore scale is much larger than the cross-shore one. The equations of motion, continuity and mass conservation give the following pressure equation:

$$p_{xxt} + f^2\left(N^{-2}p_{zt}\right)_z = 0, \qquad (1)$$

where t is the time, p the perturbation pressure, f the Coriolis parameter, and $N(z)$ is the buoyancy frequency. Subscripts indicate partial differentiation. The boundary conditions are as follows;

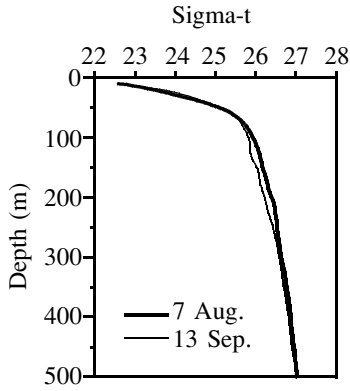$$gp_z + N^2 p = 0 \qquad \text{at } z = 0, \qquad (2)$$

Fig. 6. Vertical profiles of sigma-t observed in Sagami Bay at Sta. C on 7 August (thick line) and at Sta. D on 13 September (thin line) 2003.

$$fp_y + p_{xt} = 0 \qquad \text{at } x = 0, \qquad (3)$$

$$f^2 p_{zt} + N^2\left(fp_y + p_{xt}\right)h_x = 0 \quad \text{at } z = -h, \qquad (4)$$

$$p = 0 \qquad \text{at } x = \infty, \qquad (5)$$

where $h(x)$ is the water depth and g is the gravitational acceleration. Here, we assume the following wavelike solutions propagating the alongshore direction;

$$p = \sum_{n=1}^{\infty} F_n(x,z)\exp\left(i\left(l_n y + \omega t\right)\right) \quad n = 1, 2, ..., \qquad (6)$$

where ω is the frequency, $F_n(x, z)$ the mode structure of the n-th mode, and l_n is the wavenumber of the n-th mode. Adopting Eq. (6) for Eqs. (1)–(5) gives an eigenvalue problem for the pressure equation of $F_n(x, z)$, which is solved by using a resonance iteration method based on the algorithm of Brink and Chapman (1987). The velocity and density fields are then computed from the pressure field.

The CTWs caused by typhoons do not show a noticeable period, but the spectral analysis of the current record throughout the observation period revealed the dominance of a 6-day period. Furthermore, the current structures of CTW mode longer than 3-day period are almost independent of the period. Thus the structures and properties of CTW modes with 6-day period were investigated in the present study. The density profile obtained at Sta. C on 7 August was very similar to that at Sta. D on 13 September (Fig. 6). The buoyancy frequency, $N^2(z)$, is estimated from the averaged density profile of 7 August and 13 September in Sagami Bay, and is shown in Fig.
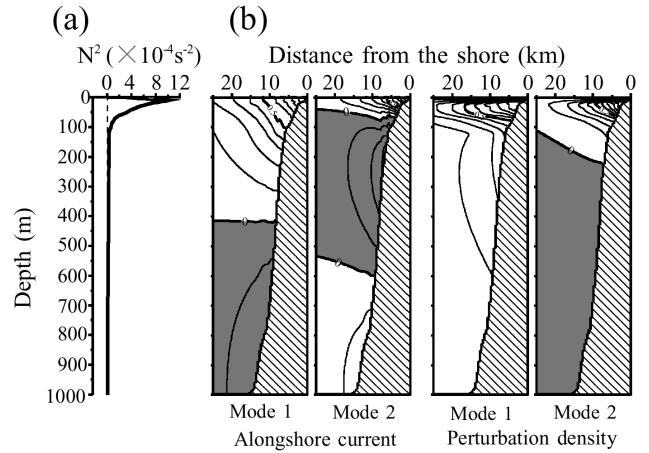

Fig. 7. (a) Vertical profile of buoyancy frequency. (b) Cross sections of alongshore current and perturbation density for the first and second CTW modes along Line I. Shaded areas indicate the negative values.

7(a). The bathymetry along Line I (Fig. 1) was applied to the calculation of the modal structure. The value of the Coriolis parameter was taken to be 8.37×10^{-5} s^{-1} at 35°N.

Figure 7(b) shows the cross-sections of the alongshore current velocity and perturbation density of CTW for the first and second mode CTWs. The values in each figure were normalized by maximum values. The alongshore current of the first-mode CTW had a node at about 400 m depth. The large current amplitude was found in the surface layer on the shelf, while the current amplitude was very small below 400 m depth. The maximum of density variations was found around the seasonal pycnocline. The alongshore current of the second-mode CTW had two nodes at about 80 m and 600 m depths. The variations of the current and perturbation density were limited in the shallower depth than about 300 m depth for both the first and second modes.

CTW has characteristics of both a continental shelf wave and an internal Kelvin wave. Brink (1982) classified the characteristics of the CTW by the ratio R (=KE/PE) of the kinetic energy KE to potential energy PE. The CTW has characteristics of a continental shelf wave when $R > 10$, while it has characteristics of an internal Kelvin wave when $R \approx 1$. In our observations, the ratio was estimated to be 1.6 and 1.3 for the first and the second CTW modes, respectively. Then CTW was expected to have the characteristics of an internal Kelvin wave in Sagami Bay.

The modal analysis gave the phase speed of the first CTW mode as 1.5 m s^{-1} and the second CTW mode as 0.8 m s^{-1}. On the other hand, the propagation speeds of the sea level fluctuations were estimated as 1.6 m s^{-1} for CTW15 and 1.3 m s^{-1} for CTW10 from the sea level data
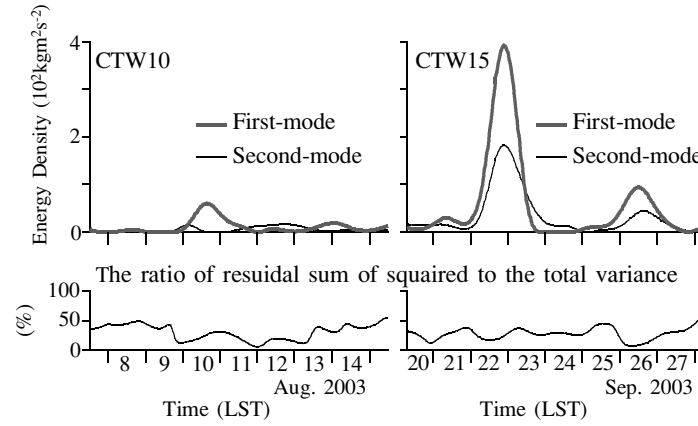
Fig. 8. Time variations of the energy density of the first and the second CTW mode due to CTW10 (left) and CTW15 (right) estimated by least squares regression using observed current record (upper panel). Time series of the ratio of residual sum of squares to total variance (lower panel).

observed at the tidal stations along the coast. The phase speeds of the sea level fluctuations of both CTW15 and CTW10 almost agree with that of the first CTW mode estimated from the density profiles in Sagami Bay.

Mode fitting of current structure of CTW mode to the observational data was performed by least squares regression, and only the two lowest modes were used for simplicity. The current observations were done at two stations and the data were obtained across the shallower node for the second-mode. Figure 8 shows the time variations of energy density for the lowest two modes and residual sum of squares during each typhoon's passage. About 75% of the observed current variance was occupied by the lowest two CTW modes during the periods of strong currents due to both CTW10 and CTW15. The first CTW mode dominates over the second mode for the CTW10, whereas both CTW modes have a significant energy level for CTW15. These results indicate that the modal characteristics of CTW15 are different from those of CTW10. However, it is difficult to justify the explanation that the difference in modal characteristics of CTWs is induced by difference of signs of wind stresses. We performed numerical experiments to understand the current structure in the generation and propagation process of CTW10 and CTW15, and discuss the difference between both CTWs.

4. Numerical Model

4.1 Model and conditions

A three-dimensional level model is applied to explain the observed features, as mentioned in the previous sections. Under the β-plane, hydrostatic and Boussinesq approximations, the equations of motion, continuity and density for an incompressible fluid are written as follows;

$$\mathbf{u}_t + \mathbf{u} \cdot \nabla_h \mathbf{u} + w\mathbf{u}_z + f\mathbf{k} \times \mathbf{u} = -\rho_0^{-1}\nabla_h p + A_h \nabla_h^2 \mathbf{u} + A_v \mathbf{u}_{zz}, \tag{7}$$

$$\rho g = -p_z, \tag{8}$$

$$\nabla_h \cdot \mathbf{u} + w_z = 0, \tag{9}$$

$$\rho_t + \mathbf{u} \cdot \nabla_h \rho + w\rho_z = K_h \nabla_h^2 \rho + K_v \delta^{-1} \rho_{zz}, \tag{10}$$

where $\nabla_h = \boldsymbol{i}\partial/\partial x + \boldsymbol{j}\partial/\partial y$, $\boldsymbol{i}$ and $\boldsymbol{j}$ the unit vectors of x (eastward) and y (northward) axes, respectively, $\mathbf{k}$ the unit vectors of z (upward), $\mathbf{u} = (u, v, w)$ the current velocity vector, u, v and w are velocity components of the eastward (x), northward (y), and vertical upward (z), respectively, t the time, f the Corioris parameter, p the perturbation pressure, g the gravitational acceleration (9.8 m s^{-2}), A_h and A_v the coefficients of the horizontal and vertical viscosity, respectively, K_h and K_v the coefficients of the horizontal and vertical diffusivities, respectively, and ρ the density, $\rho = \rho_0 + \rho'$, ρ_0 the basic density, and ρ' the perturbation density. Subscripts indicate partial differentiation. The symbol δ is the instantaneous convective adjustment parameter, which is used to maintain stable stratification in the model (e.g. Suginohara, 1982). It is defined as follows,

$$\delta = \begin{cases} 1 & \text{for } \rho_z \leq 0 \\ 0 & \text{for } \rho_z > 0. \end{cases} \tag{11}$$

The boundary condition at the sea surface ($z = 0$) is adopted as follow,

$$A_v\left(\frac{\partial u}{\partial z}, \frac{\partial v}{\partial z}\right) = C_s \frac{\rho_a}{\rho_0} W\left(W_x, W_y\right) \quad \text{at } z = 0, \quad (12)$$

where $W = (W_x^2 + W_y^2)^{1/2}$ is the wind speed, and W_x and W_y are the eastward and northward components of wind velocity in the x and y directions, respectively, and ρ_a the density of air, and C_s the coefficient of wind stress ($C_s = 0.0016$). The boundary condition at the sea bottom ($z = -H$) is adopted as follow;

$$A_v\left(\frac{\partial u}{\partial z}, \frac{\partial v}{\partial z}\right) = C_b U_b\left(u_b, v_b\right) \quad \text{at } z = -H, \quad (13)$$

where $U_b = (u_b^2 + v_b^2)^{1/2}$ is the bottom current, and u_b and v_b are the eastward and northward components of velocity in the x and y directions, respectively, and C_b is the coefficient of bottom friction ($C_b = 0.0026$).

Equations (7)–(10) were approximated by finite difference equations. The centered difference was applied to spatial difference using the Arakawa C grid. A leapfrog scheme was adopted for time difference. The Euler-backward scheme was used every 20 time steps to avoid numerical instability. The other parameters were as follows; $\rho_a = 1.2$ kg m^{-3}, $A_v = 0.002$ m^2 s^{-1}, $K_h = 100$ m^2 s^{-1}, $K_v = 0.001$ m^2 s^{-1}, and A_h was calculated with a Smagorinsky eddy parameterization (multiplier 0.2).

Figure 9 shows the model ocean of 700 km from north to south and 700 km from east to west. JTOPO30 (Marine Information Research Center) is applied for the topographic data. Depths deeper than 1000 m was set to 1000 m in order to focus on the phenomena in the coastal region (Kitade and Matsuyama, 2000; Igeta *et al.*, 2003). The grid size was 2 km × 2 km horizontally, and the grid points were set at constant depth in z-level, that is, ten vertical levels were set at depths of 5, 15, 30, 50, 80, 140, 230, 380, 580 and 840 m. These grid sizes were based on the need to carry out the calculation using remarkable wind stress and for adequate resolution of the internal radius of deformation ($NH/f \sim 15$ km, where H the maximum depth of the model ocean). The clamped condition was adopted at open boundaries to allow surface Ekman transport across the open boundary (Chapman, 1985). In addition, the sponge condition was applied along the open boundaries to reduce the disturbance. The slip condition was adopted along the open boundaries, while the nonslip condition was used along the rigid boundaries.

The model ocean was assumed to be at rest initially. The density distributions observed in Sagami Bay in September and August (Fig. 6) were applied for the basic density fields. The wind forcing conditions related to the passage of T15 and T10 were used for Exp. 1 and Exp. 2, respectively. The wind stress of the computational domain was constructed by spatially optimum interpolation
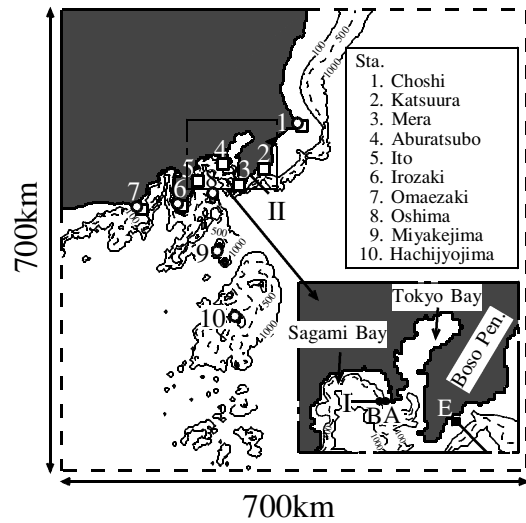

Fig. 9. Computational domain. Realistic coastline and bottom topography is used in this study. Depths greater than 1000 m were set to 1000 m. Location of meteorological and tidal stations are indicated by open circles and open squares, respectively. Mooring observation sites are indicated by closed circles. Modal structures are investigated along Lines I and II.

of the wind data at the five meteorological observatories as shown in Figs. 1 and 9. The wind data of 10 days, including before and after the typhoon passage, was applied in each experiment.

4.2 Generation and propagation processes of coastal-trapped wave

Generation process of CTW15

The horizontal distributions of perturbation density and current vector at 15 m depth from 60 to 160 hours in the case of Exp. 1 are shown in Fig. 10. The inertial motion is already removed by a 21-hours running average. The southward wind associated with T15 is gradually strengthened from the initial state, and its magnitude reaches the maximum at 100 hours at Choshi. The shoreward Ekman transport is induced by the southward wind along both the eastern coast of the Boso Peninsula and the western side in Sagami Bay, and a remarkable downwelling is formed in both regions at 80 hours. From 80 to 120 hours the downwelling moves along the coast of the Boso Peninsula on the right with the strong alongshore current. The downwelling intrudes into Sagami Bay by bridging over the mouth of Tokyo Bay. The strong inflow is induced at 15 m depth around the observed area in Sagami Bay by CTW15, and forms cyclonic circulation in Sagami Bay. CTW15 propagates into Suruga Bay after 160 hours and the downwelling is gradually reduced as the wind decreased.
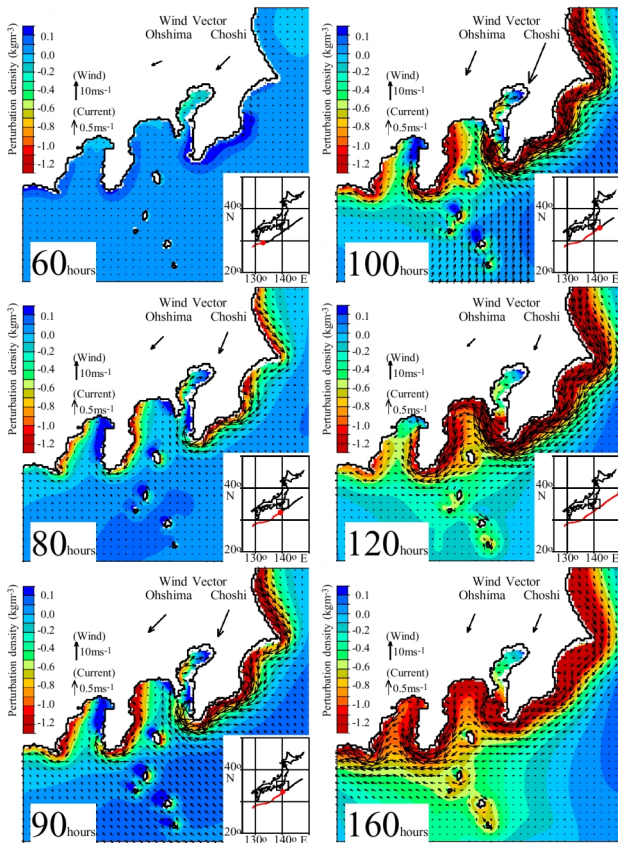
Fig. 10. Horizontal distributions of 21-h running averaged perturbation density and current vector at 15 m depth in Exp. 1 (Experiment for T15). Wind vector at Choshi and Oshima are also shown. Insets show the locations of the centers and tracks of typhoon.

Fig. 11. As Fig. 10 but for Exp. 2 (Experiment for T10). Insets show locations of the centers and tracks of typhoon.

Generation process of CTW10

Figure 11 shows the horizontal distributions of perturbation density and current vector at 15 m depth from 80 to 200 hours in the case of Exp. 2. The maximum wind at Choshi occurs at 111 hours in the model. The upwelling region is formed along the eastern coast of the Boso Peninsula and the western side of Sagami Bay by the northward wind at 110 hours. On the other hand, the downwelling is formed in Tokyo Bay, at the head of Sagami Bay, and the eastern coast of Suruga Bay. At 130 hours, the upwelling along the Boso Peninsula is strengthened and is accompanied by the northeastward alongshore currents. The alongshore current region then extends from the Boso Peninsula to Sagami Bay, that is, the outflow at 15 m depth is formed on the eastern side of Sagami Bay. The current field near the coast propagates westward along the bay coast, while the upwelling and downwelling regions formed along the coast do not propagate clearly. The currents due to CTW10 are weak at 15 m depth in comparison to that of CTW15.
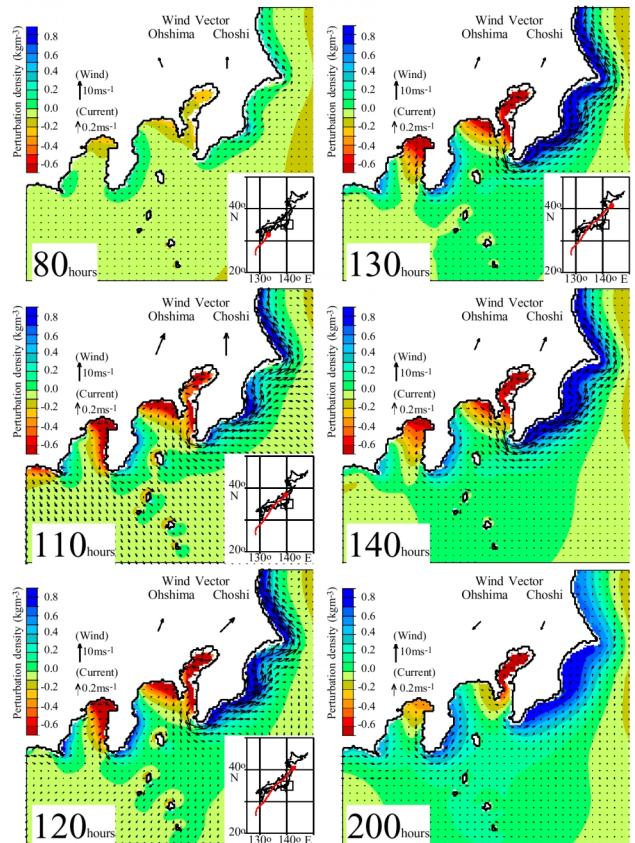
Propagation properties of CTW15 and CTW10

As shown in Figs. 10 and 11, the model results show a remarkable difference in the properties of CTW15 and CTW10. Propagation of CTW10 cannot easily be found in the horizontal distributions of perturbation density at 15 m depth. We thus investigated the propagation properties of CTW at different depths. The propagation signals of CTW15 and CTW10 appear as negative and positive perturbation densities, respectively. Therefore, we show the horizontal distributions of minimum perturbation densities due to CTW15 and of maximum ones due to CTW10 at 15 m and 140 m depths in Fig. 12. Each value is obtained from 0 to 200 hours. The absolute values of perturbation density at 15 m depth due to CTW15 gradually decrease in the offshore direction from the coast, and toward the west from the Boso Peninsula, which shows the westward propagation of CTW15 along the coast (e.g. Igeta *et al.*, 2003). The density distribution at 140 m depth for CTW15 is similar to that at 15 m depth. The westward propagation signal of CTW15 appears at 140 m depth, too. For CTW10, the remarkable upwelling region associated with CTW10 generation is found in the
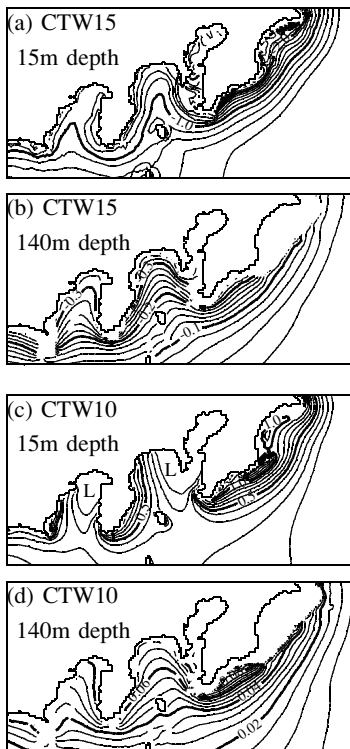
Fig. 12. Horizontal distribution of minimum perturbation density obtained from 0 to 200 hours for (a) at 15 m depth and (b) at 140 m depth in Exp. 1. (c) and (d) are the same as (a) and (b), but for maximum perturbation density in Exp. 2. Numerals on the contour lines are in kg m^{-3}.

density distribution at 15 m depth around the eastern coast of the Boso Peninsula. Upwelling regions are also found at the western part of Sagami and Suruga Bays, whereas no upwelling region distributes on the eastern side of the Bays. The clear propagation properties of CTW10 are not found at 15 m depth. On the other hand, the spatial upwelling pattern at 140 m depth for CTW10 is similar to that for CTW15, which indicates that CTW10 propagation is accompanied by upwelling at 140 m depth. Moreover, local responses to the wind, i.e., downwelling, on the eastern side of Sagami and Suruga Bays were considered to exceed the upwelling due to CTW10 at 15 m depth. These phenomena are considered to result from the fact that the upwelling region does not propagate westward from the eastern coast of the Boso Peninsula at 15 m depth.

5. Discussion

5.1 Comparison of numerical experiments with observations

The current and temperature structures of CTW obtained by the numerical experiments were compared with the observed structures. Figure 13 shows the comparison of model results of CTW15 with the observations. The observed features of CTW15 are as follows: (1-A) the strong inflow throughout the water column at Sta. A; (1-B) the strong inflow concentrated above 90 m depth at Sta. B; (1-C) the remarkable downwelling throughout the water column at Sta. B; (1-D) the westward propagation of the sea level elevation. The qualitative reproducibility of (1-A)–(1-D) were considered to be good. However, in terms of (1-A), the vertical attenuation of the inflow of the model is larger than the observed value. Table 1 indicates the maximum velocity at the representative depths of Stas. A and B obtained by both the observations and numerical experiments, and the ratio of both values. The current velocity at 15 m and 30 m depths due to CTW15 in the model is about 80% of the observed value. However, the current velocity below 50 m depth in the model is less than 40% of that of the observed value. Table 2 presents time lags between the maximum wind at Choshi and maximum alongshore current according to both the models and observations. The currents at both stations for CTW15 lag by 12 to 21 hours behind the wind for the observations and by 13 to 21 hours for the model. No systematic relations can be found in differences of the time lag as between the model and observation. The mean speed of the westward propagation of sea level elevation is about 1.3 m s^{-1} in the model, whereas the observed value is 1.6 m s^{-1}. The model result is slightly low in comparison with the observed results.

On the other hand, Fig. 14 shows the comparison of model results of CTW10 together with the observations. The observed features of CTW10 are as follows: (2-A) the outflow intensified near the bottom at Sta. A; (2-B) the outflow throughout the water column at Sta. B; (2-C) the upwelling only near the bottom at Sta. B; (2-D) the westward propagation of the sea level depression. The features of (2-A)–(2-D) are qualitatively reproduced by the numerical model. However, the bottom intensification of the outflow—i.e., weak outflow near the sea surface—is not reproduced adequately at Sta. A. The current velocity at 50 m depth at Sta. A obtained by the numerical model is about 70% of the observed value, whereas the current velocities at 80 m depth at Stas. A and B given by the model are less than 30% of the observed values (Table 1). The currents at both stations for CTW10 lag by 24 to 29 hours behind the wind for the observation and by 18 to 26 hours for the model (Table 2). The differences in the time lags are 2 to 8 hours as between the observation and model for CTW10, and the lags at Sta. A are less than those of Sta. B. The mean speed of the westward propagation of sea level depression is 1.1 m s^{-1} in the model and 1.3 m s^{-1} according to observation, so the former is slightly slower than the latter.

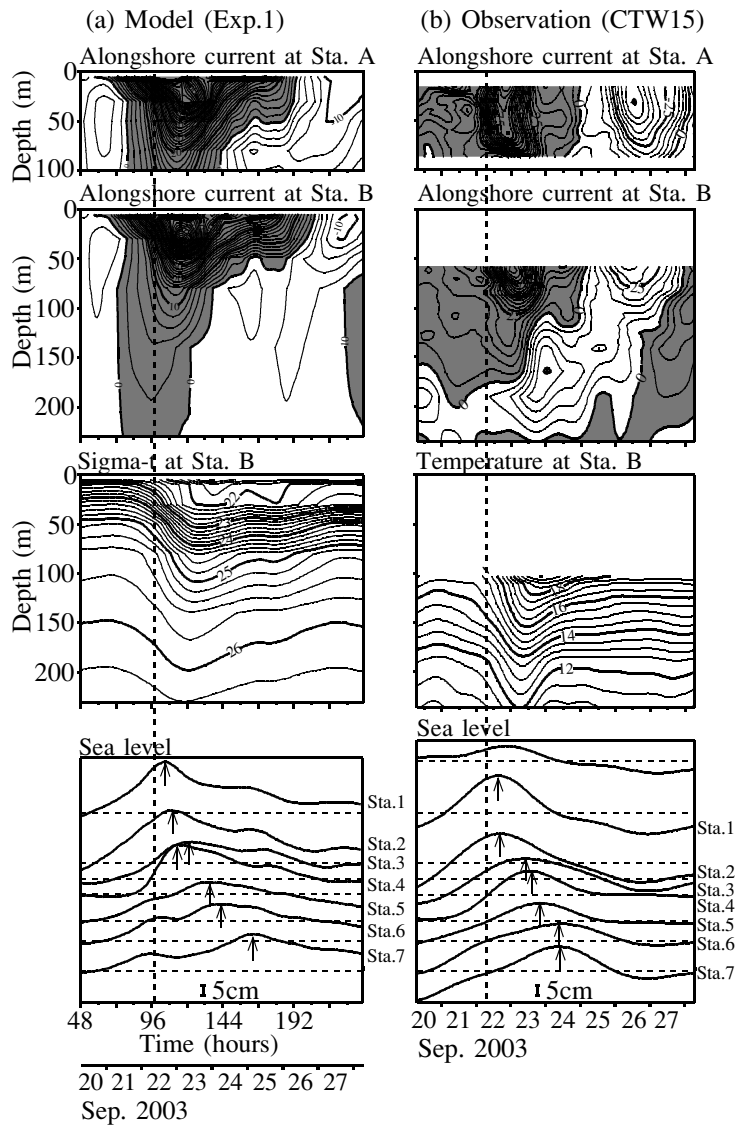(a) Model (Exp.1)   (b) Observation (CTW15)

Fig. 13. (a) Time variations of alongshore current at Stas. A and B, and sigma-t variation at Sta. B, time series of sea level at each tidal station due to CTW15 in the model (Exp. 1). Fluctuations associated with inertial motion were removed by 21-hour running average. Observational results at Stas. A and B during CTW15 propagation are added in (b). Shaded areas indicate the inflow into Sagami Bay. Dashed lines show maximum wind speed at Choshi.

Table 1. Maximum alongshore velocity due to CTW15 and CTW10 at the representative depths of Stas. A and B obtained by both observations and calculations and ratio of both values. Numerals are in cm s^{-1}.

	CTW15			CTW10		
	Obs. (V_o)	Model (V_m)	Ratio (V_m/V_o)	Obs. (V_o)	Model (V_m)	Ratio (V_m/V_o)
Sta. A 15 m	98.6	78.8	0.80	—	—	—
Sta. A 30 m	88.2	73.2	0.83	—	—	—
Sta. A 50 m	83.8	41.7	0.50	14.4	10.0	0.69
Sta. A 80 m	58.9	21.1	0.36	28.2	7.4	0.26
Sta. B 50 m	91.8	35.5	0.39	22.5	4.9	0.22
Sta. B 80 m	68.4	11.6	0.17	23.3	2.8	0.12

Table 2. Time lags between the maximum wind at Choshi and maximum alongshore current due to CTW15 and CTW10 of the models and observations. Numerals are in hours.

	CTW15			CTW10		
	Obs. (TL_o)	Model (TL_m)	Difference ($TL_m–TL_o$)	Obs. (TL_o)	Model (TL_m)	Difference ($TL_m–TL_o$)
Sta. A 15 m	14.0	13.0	−1.0	—	—	—
Sta. A 30 m	12.0	21.0	9.0	—	—	—
Sta. A 50 m	13.0	18.0	5.0	28.0	26.0	−2.0
Sta. A 80 m	19.0	15.0	−4.0	24.0	26.0	2.0
Sta. B 50 m	17.0	19.0	2.0	29.0	21.0	−8.0
Sta. B 80 m	21.0	17.0	−4.0	25.0	18.0	−7.0
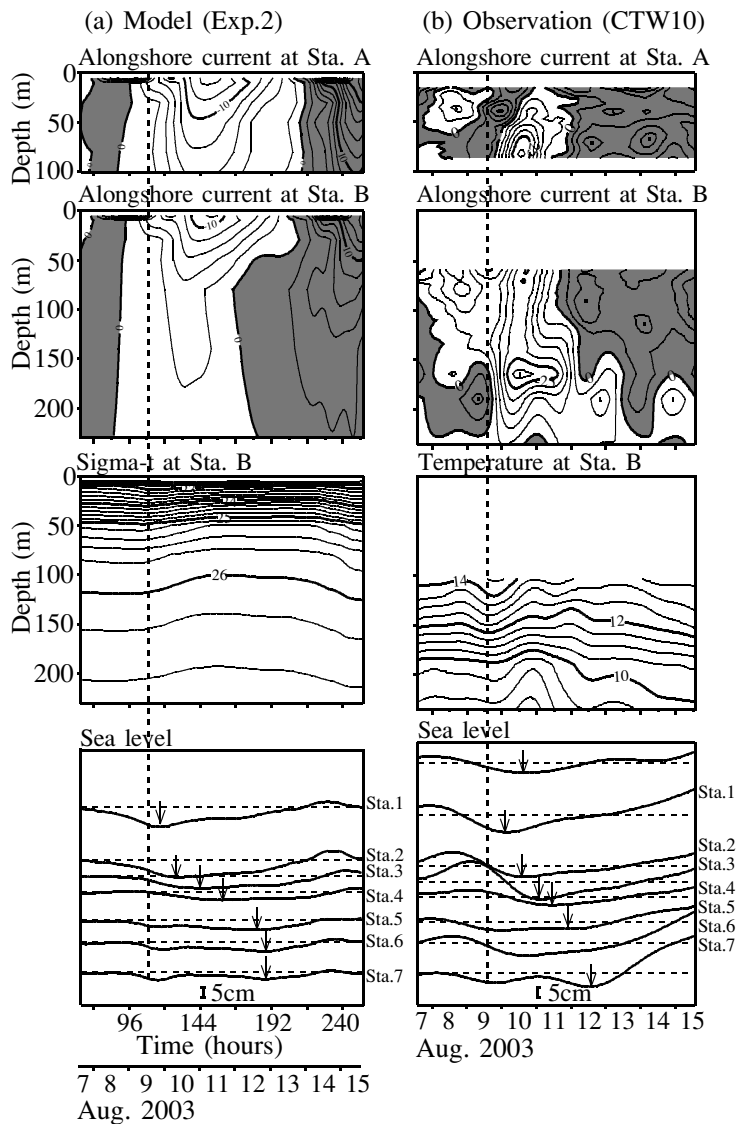
Fig. 14. (a) As Fig. 13(a), but for Exp. 2. (b) As Fig. 13(b), but for CTW10.
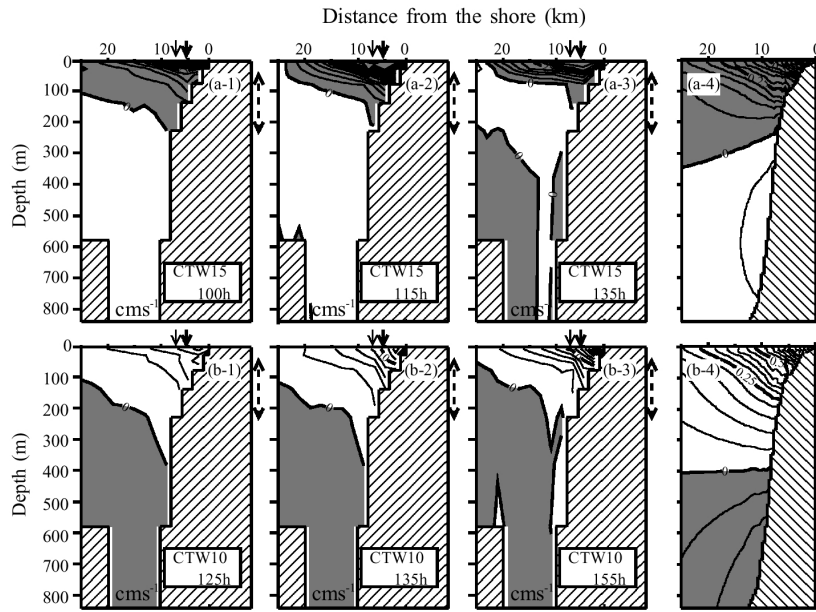
Distance from the shore (km)

Fig. 15. Cross sections of northward current on Line I. Upper panels (a-1, a-2, a-3) are from Exp. 1 and lower panels (b-1, b-2, b-3) are from Exp. 2. Shaded areas indicate northward current. Thick and thin arrows indicate locations of Stas. A and B, respectively. Dashed arrows indicate the observation layers at Sta. B. (a-4) and (b-4) are alongshore current structures estimated by sum of the lowest two CTW modes with observed amplitude ratio for CTW15 and CTW10, respectively. The ratio of the first mode to the second mode was about 1.4 in case of CTW15 (a-4) and about 5.0 in case of CTW10 (b-4).

As mentioned above, the model results agree with the observational ones qualitatively, but several disagreements exist in terms of quantitative characteristics in these numerical experiments. The discrepancies of the current velocity as between the observation and model are considered to depend on the vertical and horizontal resolution for the numerical experiments. These problems remained for future study.

The main features of the model results agree well with the observational ones, although several simplifications were applied to the physical conditions in the numerical models. The quantitative reproducibility of the observational CTWs properties is quite good above 50 m depth. Judging from the above discussion, we can conclude that the experimental results are useful for the discussions of modal characteristics of CTWs.

5.2 Formation process of different structures of CTW

We investigated the difference of modal characteristics between CTW10 and CTW15 using the numerical experimental results. The experimental results should be decomposed into several CTW modes. However, the complication of horizontal variation of the bottom topography and the coarse vertical resolution of the numerical model prevented us from performing the modal decom-

position. We therefore infer the modal characteristics of CTWs from the description of the current structure of reproduced CTWs. Figure 15 shows the cross sections of northward current along Line I in Sagami Bay (see Fig. 9) in both Exp. 1 and Exp. 2; three cross sections are drawn at three different times. The structure of the northward current due to CTW15 expresses the inflow above 200 m depth and outflow below 200 m depth. The thickness and width of the inflow in the upper layer gradually decreases with time from 100 to 135 hours. In Exp. 2 for CTW10, the model results describe the outflow above 400 m depth and inflow below 400 m depth. The isolines cross diagonally on the continental slope, so the current is almost uniform vertically around the observation area.

The modal structures of CTW estimated from the observed density profiles and the bottom topography (Fig. 7) are applied to the model results to understand the complicated vertical distributions along the Line I. Alongshore current structures were estimated by the sum of the lowest two CTW modes with observed amplitude ratio (Figs. 15(a-4) and (b-4)). The ratio of the first mode to the second mode was about 1.4 in case of CTW15 and about 5.0 in case of CTW10. The current structures of CTW15 at 100 and 115 hours (Fig. 15) resemble the structure shown in (a-4), so it is expected to be affected by both the first
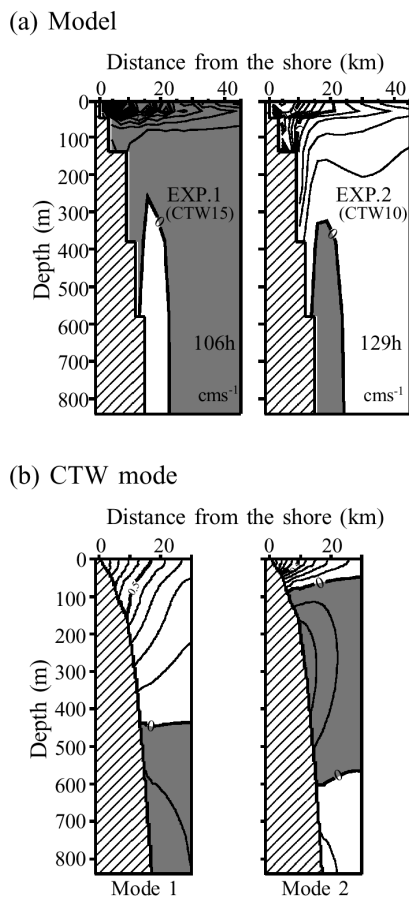
(a) Model

(b) CTW mode

Fig. 16. (a) Cross sections of alongshore current along Line II at the time of maximum current at 15 m depth of Sta. E (Fig. 9) in Exp. 1 (left) and Exp. 2 (right). (b) Cross sections of alongshore current of the first (left) and the second CTW mode (right) along Line II estimated by using the method of Brink and Chapman (1987).

Fig. 17. Cross sections of sigma-t along Line II at the time of maximum current at 15 m depth of Sta. E in Exp. 1 (left) and Exp. 2 (right).

and second CTW mode in Line I. The contribution of the second CTW mode (Fig. 7) to CTW15 becomes strong with increasing time. The current structure due to CTW10 is similar to the structure shown in (b-4) in Line I at all times. These results indicate the difference of modal characteristics between CTW15 and CTW10, that is, CTW15 is constructed by both the first and second CTW modes, whereas CTW10 is mainly explained by the first CTW mode.

The difference of the modal characteristics between CTW15 and CTW10 in Sagami Bay is investigated to see whether or not a difference is already apparent along the eastern coast of the Boso Peninsula, i.e., the generation region of CTWs. Figure 16(a) shows the cross sections of alongshore current along Line II (Fig. 9) in both Exp. 1 and Exp. 2. The time in each section coincides with that of maximum current speed at 15 m depth at Sta. E
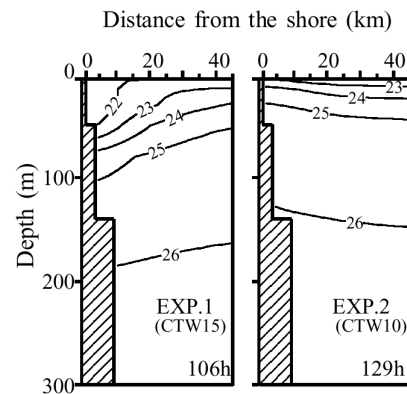
(Fig. 9). The strong current due to CTW15 concentrates near the coast above 100 m depth along Line II, so the baroclinicity is quite strong. The current distribution due to CTW10 indicates that the coastal-trapped structure and the isolines of currents are less different vertically near the shore, so the baroclinicity is relatively weak. The properties of CTW15 and CTW10 in Sagami Bay are already similar to those along the eastern coast of the Boso Peninsula, i.e., the generation region.

Figure 16(b) shows the cross sections of alongshore current of the first and second CTW modes along Line II of the Boso Peninsula, estimating from the observed density profile in Sagami Bay by the method of Brink and Chapman (1987). Along Line II, the current structures of CTW15 agree with the second CTW mode above 100 m depth, and resemble the first CTW mode below 400 m depth, and those of CTW10 resemble the first CTW mode. This indicates that the modal characteristic of CTW15 was different from that of CTW10 in the generation region, that is CTW15 is explained by superposing the second CTW mode on the first CTW mode, whereas CTW10 is mostly formed by the first CTW mode.

We tried to find the cause of the difference in modal characteristics of CTW by investigating the density stratification in the CTW generation region. Figure 17 shows the cross sections of sigma-t along Line II in Exp. 1 and Exp. 2. The downwelling structure is formed in the case of CTW15 near the coast in Exp. 1, whereas the upwelling structure is formed in the case of CTW10. The isopycnal surface of sigma-t = 23 reaches to the sea surface as a result of the remarkable upwelling due to CTW10. Therefore, the subsurface water outcrops, so the density stratification in the surface layer near the coast is weak in comparison with the case of CTW15. Thus, the weak generation of the second CTW mode related to CTW10 is con-

sidered to result from the weak density stratification in the surface layer near the coast in the case of CTW10 compared with that in the case of CTW15. These results imply the possibility that the modal characteristics of CTWs depend on the wind direction along the eastern coast of the Boso Peninsula. Nevertheless, the discussion of a detailed mechanism is beyond this paper. The clarification of modal characteristics of large amplitude CTW under a continuously stratified condition remains a problem for the future.

6. Summary

In Sagami Bay, Japan (Fig. 1), strong currents associated with a CTW have often been observed at the mooring stations near the coast about one day after the passage of a meteorological disturbance (e.g. Matsuyama *et al.*, 1997; Kitade *et al.*, 1998; Ishidoya, 2001). To clarify the detailed structure of the current due to the CTW in the coastal region of Sagami Bay, mooring observations using ADCP, ACM, memory thermometers and temperature-depth meters were carried out on the shelf and the continental slope on the eastern side of Sagami Bay from 28 July to 6 October 2003.

The strong currents associated with CTW were observed after the passage of two typhoons, i.e., T10 and T15. The CTWs were induced off the eastern part of Boso Peninsula by the strong alongshore wind related to the typhoons and they propagated with the currents and temperature variations into Sagami Bay. CTW15 associated with coastal downwelling was caused by the southward wind of T15 passing south off the bay, and caused the inflow above 90 m depth at mooring stations in Sagami Bay. The maximum current due to CTW15 was over 100 cm s^{-1}, concentrated in depth shallower than 90 m. CTW10 induced by T10 passing on the land was associated with the coastal upwelling by the wind left on the Boso Peninsula, and the maximum current was only 33 cm s^{-1}, but the currents were uniformly extended near the bottom of 230 m depth. CTW15 is explained by superposing the second CTW mode on the first CTW mode, whereas CTW10 was explained by the first CTW mode. The generation and propagation processes of both CTWs were reproduced by numerical experiments using a three-dimensional level model with realistic bottom topography, stratification condition, and wind fields. The model results indicate that the difference of modal characteristics between both CTW15 and CTW10 already exists in the generation region. The remarkable change of the density structure due to strong wind stress in the generation region was considered to be the cause of the difference in mode characteristics of CTWs. Clarification of modal characteristics of large amplitude CTW under the continuously stratified condition remains a problem for the future.

References

Brink, K. H. (1982): A comparison of long coastal trapped wave theory with observations off Peru. *J. Phys. Oceanogr.*, **12**, 897–913.

Brink, K. H. and D. C. Chapman (1987): Programs for computing properties of coastal-trapped waves and wind-driven motions over the continental shelf and slope. *WHOI Tech. Rep.* 87-24, 2nd ed., Woodshole Oceanographic Institution, Woods Hole, MA, 119 pp.

Chapman, D. C. (1985): Numerical treatment of cross-shelf open boundaries in a barotropic coastal ocean model. *J. Phys. Oceanogr.*, **15**, 713–748.

Gill, A. E. (1982): *Atmosphere–Ocean Dynamics*. Academic Press, Inc., Orlando, 662 pp.

Hanawa, K. and H. Mitsudera (1985): On the data processing of daily mean values of oceanographical data—Note on daily mean sea level data. *Bull. Coast. Oceanogr.*, **23**, 79–87 (in Japanese).

Igeta, Y., Y. Kitade and M. Matsuyama (2003): Numerical experiments on the Kyucho current in Sagami Bay associated with the coastal-trapped waves caused by typhoon 8818. *Oceanogr. in Japan*, **12**, 603–617 (in Japanese with English abstract).

Ishidoya, H. (2001): Studies on Kyucho events and disaster prevention of set nets in Sagami Bay. *Special Report of the Kanagawa Prefectural Fisheries Research Institute*, Vol. 1 Miura, Japan (in Japanese with English abstract).

Kajiura, K. (1974): Effect of stratification on long period trapped waves on the shelf. *J. Oceanogr. Soc. Japan*, **30**, 271–281.

Kitade, Y. and M. Matsuyama (2000): Coastal-trapped waves with several-day period caused by wind along the southeast coast of Honsyu, Japan. *J. Oceanogr.*, **56**, 727–744.

Kitade, Y., M. Matsuyama, S. Iwata and I. Watabe (1998): SDP and LP fluctuations observed along the coast of Sagami Bay. *J. Oceanogr.*, **54**, 297–312.

Kubota, M. (1985): Continental shelf waves off the Fukushima coast. Part 3. Numerical experiments. *J. Oceanogr. Soc. Japan*, **41**, 105–112.

Kubota, M., K. Nakata and Y. Nakamura (1981): Continental shelf waves off the Fukushima coast. Part 1: Observations. *J. Oceanogr. Soc. Japan*, **37**, 267–278.

Matsuyama, M., S. Iwata and H. Nagamatsu (1997): Kyuchyo in Sagami Bay induced by Typhoon 8818. *J. Oceanogr.*, **53**, 199–205.

Suginohara, N. (1982): Coastal upwelling: Onshore-offshore circulation, equatorward coastal jet and poleward undercurrent over a continental shelf-slope. *J. Phys. Oceanogr.*, **12**, 272–284.

Walters, R. A. and C. Heston (1982): Removing tidal period variations from time series data using low-pass digital filters. *J. Phys. Oceanogr.*, **12**, 112–115.

Wang, D.-P. and C. N. K. Mooers (1976): Coastal-trapped waves in a continuously stratified ocean. *J. Phys. Oceanogr.*, **6**, 853–863.